A hierarchical, spherical harmonic-based approach to simulate abradable, irregularly shaped particles in DEM

A hierarchical, spherical harmonic-based approach to simulate abradable, irregularly shaped particles in DEM

R. Capozza*, K. J. Hanley

School of Engineering, Institute for Infrastructure and Environment, The University of Edinburgh, Edinburgh EH9 3JL, United Kingdom

Abstract

A novel approach is presented for simulating non-spherical particles in the discrete element method (DEM). A particle's shape is described through a hierarchy of representations using spherical harmonic expansions. The expansion is computed at nodes, obtained by discretising the particle's surface. A low-degree expansion, i.e., one containing few terms, is sufficient to approximate a particle's overall shape without any surface texture. Expansions are computed to high degrees only at interparticle contacts, rather than for the entire particle, which reduces the computational cost. The advantages of this approach include the ability to simulate a wide range of particle shapes and adaptive resolution depending on spatial and temporal considerations. An additional unique benefit is that changes of particle shape due to chipping can be captured in DEM for the first time. This is accomplished by progressively omitting more of the highest-degree terms from the expansion to give an increasingly smooth surface.

Keywords: Discrete element method (DEM), Adaptive resolution, Contact

*Corresponding author.
Email address: rcapozza@exseed.ed.ac.uk (R. Capozza)

detection, Abrasion, Attrition

1. Introduction

Particle shape plays a fundamental role in the statics, dynamics and resistance to attrition of granular materials. It affects the height and porosity of a static bed of particles [1]. Particle shape affects the angle of repose in both a quasi-static sandpile [2, 3] and a rotating drum [4, 5]. In dynamic systems, variability in particle shape can induce segregation [6, 7] or affect flow rates [8, 9], mechanical behaviour [10, 11] or the particles' wearing propensity [12–14].

Despite the recognised importance of particle shape, spheres have often been used to represent particles in discrete element method (DEM) simulations, irrespective of their real shapes. Spheres have the great advantage of computational simplicity: straightforward contact detection, orientation independence and low memory requirements. However, spheres are often inadequate if quantitative agreement with a real, physical system is sought. Increasing computational resources have encouraged a commensurate increase in research activity in the modelling of granular systems composed of non-spherical particles in recent years [15–17].

The simplest option, though often inadequate [18, 19], is to combine spheres with a rotational resistance model which imposes torque terms at each interparticle contact to inhibit rolling and twisting motions. Replacing spheres with ellipsoids [20] or superquadrics [21] – a generalisation of ellipsoids – introduces non-sphericity but is limited to a subset of symmetrical shapes. Representing particles using polyhedra allows sharp edges and flat

surfaces to be simulated [22–24], but not in combination with curved surfaces. The aforementioned are 'single-particle' methods. However, the most common approach to simulate non-spherical particles is the multi-sphere method: spheres are simply clumped together to create irregular clusters. This method is adopted in the commercial codes EDEM [25] and PFC [26]. Since spheres remain the fundamental particles, contact detection is simple [27]. However, many spheres may be required to obtain a reasonable approximation of a real particle's shape [16, 28, 29]. Many less commonplace methods have also been proposed to capture non-spherical particle shapes in DEM, e.g., non-uniform rational B-splines [30], potential particles [31, 32] and spheropolyhedrons, generated from the Minkowski sum of a polyhedron with a sphere [33].

Some of these methods are restricted to a subset of particle shapes; others such as multi-spheres or polyhedra can, in principle, be used to simulate a particle of any arbitrary shape. Advances in X-ray computed tomographic imaging have enabled the measurement of particle morphology at a very high level of detail, equivalent to 15^3–25^3 voxels per sand grain [34]. It is unlikely that such a detailed representation, captured using a very large number of polyhedron faces or spheres in a multi-sphere cluster, is needed to simulate the behaviour of most granular systems adequately. Some studies have been done for specific situations, e.g., [35], but in general the fidelity of particle shape required to obtain an acceptable bulk response remains an open question.

One of the biggest challenges in modelling non-spherical particle shapes is contact detection. Two approaches are commonly used: continuous function representation (CFR) and discrete function representation (DFR). CFR uses

non-linear and iterative methods to detect and evaluate interparticle contacts, solving the equations which describe a particle's shape [36]. In DFR [36–38], the surface of a particle is discretised into a set of surface nodes; contact detection involves evaluating whether any of these nodes lie inside a potentially contacting particle [27]. CFR and DFR can have comparable efficiency and accuracy on modern computing hardware [39]. Both are much more computationally expensive than contact detection for spheres. Therefore, a hierarchical representation of the geometry is often used to reduce the computational cost by cheaply eliminating a large proportion of non-contacts. Williams and O'Connor [38], for example, used four levels in their hierarchy: a bounding sphere, a bounding box, cellular regions and surface facets.

Another major challenge, one often ignored in DEM simulations, is changes of particle shape over time due to attrition, i.e., fragmentation or surface abrasion. Attrition is a particularly significant consideration for angular particles which are more susceptible to damage than rounded ones. The motivation for considering attrition in simulations is its industrial importance. Fines reduce flowability which can impair processing operations such as conveying, blending or tableting [40]. In the pharmaceutical sector, needle- and plate-type crystals are often produced [41]. Attrition of these crystals has major implications for product quality, affecting bulk density, specific surface area, segregation behaviour, dissolution rate and even surface chemistry [42, 43]. Attrition of infant formula disimproves the product's rehydration characteristics and affects bulk density [44]. The mechanical degradation of catalysts, which necessitates their periodic replacement, is a significant

cost factor in fluidised bed processes [45]. Particle fragmentation can be simulated in two broad ways in DEM [46–48]: (i) agglomerates, created by joining the fundamental particles (usually spheres) with bonds of finite strengths, can disintegrate upon bond failure; (ii) particles are deemed to fail when a predefined force or stress is reached, after which they are replaced with smaller 'daughter' particles. However, there is no existing method to simulate abrading particles during a DEM simulation which takes into consideration the evolving particle shape. As an alternative, DEM simulations of non-abrading particles are sometimes performed to obtain data on the relevant particle dynamics, e.g., impact velocities, forces and collision frequencies, or estimated distributions of stresses and strains. These data are subsequently used as input to attrition models [42, 49].

In this paper, a novel approach is presented for modelling abradable, non-spherical particles in DEM which has several unique advantages:

- This approach is based on spherical harmonics, so inherently contains a hierarchical description of shape from a sphere to a highly refined representation with surface texture.

- Particles can be simulated with adaptive fidelity, e.g., depending on their location within the simulation domain or the time elapsed during the simulation.

- Abrasion can be captured by progressively omitting terms from the spherical harmonic expansion.

In addition, the approach is relatively straightforward to integrate into a sphere-based code. Section 2 describes how spherical harmonics can be used

to represent particle shapes. This is used and adapted in the novel DEM simulation approach described in Sections 3 and 4, which includes a demonstration of the method with two contacting particles. Section 5 demonstrates that the approach naturally includes the evolution of particle shape due to abrasion. Finally, some discussion of efficiency and the future implementation of the approach in a suitable code (such as LAMMPS [50]) is provided in Section 6.

2. Spherical harmonics for particle shape representation

We assume that the particle does not contain any voids and is 'star-shaped', i.e., any half-line drawn from a suitable origin, O, inside the particle crosses the particle's contour exactly once. Therefore the particle can be analytically described by a function $r(\theta, \varphi)$ which is the distance from O. θ and φ are the polar angles, with $0 \leq \theta \leq \pi$ and $0 \leq \varphi \leq 2\pi$. The requirement for particles to be 'star-shaped' is rarely a limitation since a majority of natural particles fulfil this condition [51].

The function $r(\theta, \varphi)$ can be approximated as a truncated spherical harmonic series [51, 52] which is a generalisation to 3D of the Fourier series:

$$r(\theta, \varphi) \approx r_{SH}(N, \theta, \varphi) = \sum_{n=0}^{N} \sum_{m=-n}^{n} c_n^m Y_n^m(\theta, \varphi) \tag{1}$$

where $Y_n^m(\theta, \varphi)$ is the spherical harmonic function, n is the degree, m the order and N indicates the maximum degree at which the expansion is truncated. The function $Y_n^m(\theta, \varphi)$ is given by:

$$Y_n^m(\theta, \varphi) = \sqrt{\frac{(2n+1)(n-m)!}{4\pi(n+m)!}} P_n^m(\cos\theta) e^{im\varphi} \tag{2}$$

The functions $P_n^m(x)$ are called associated Legendre functions, and are a set of orthogonal polynomials widely used in quantum mechanics [53] and many other fields. If the function $r(\theta, \varphi)$ is known, the coefficients c_n^m can be calculated as

$$c_n^m = \int_0^{2\pi} \int_0^{\pi} \sin(\theta) r(\theta, \varphi) Y_n^{m*} d\theta d\varphi \tag{3}$$

where the asterisk denotes the complex conjugate. Simple geometrical shapes such as ellipsoids, cubes, etc. can be obtained by choosing a suitable set of coefficients [54], with a level of accuracy increasing with N.

Using well-known properties of spherical harmonic functions [53], it is possible to write the representation in Eq. (1) in a different form which uses real rather than complex-valued functions and coefficients:

$$r_{SH}(N, \theta, \varphi) = a_0^0 Y_0^0 + \sum_{n=1}^{N} \left[a_n^0 Y_n^0 + \sum_{m=1}^{n} P_n^m(\cos\theta) \left(a_n^m \cos(m\varphi) + b_n^m \sin(m\varphi) \right) \right] \tag{4}$$

where $Y_0^0 = \sqrt{\frac{1}{4\pi}}$. The set of coefficients $\{a_n^m\}$ and $\{b_n^m\}$ carry all the information on the particle shape.

Laser scanning and computed tomography are increasingly widely used to obtain the point cloud of a particle's surface and study the morphology characteristics of different particles in nature [55]. After converting the 3D point cloud data into polar coordinates, established techniques can be used to extract the set of coefficients of a spherical harmonic expansion [54, 56].

If the surfaces of a large number of particles are extracted from a particular sample, the statistics (or population) of coefficients $\{a_n^m\}$ and $\{b_n^m\}$ represent the 'fingerprint' of that particular sample or set of particles [56]. Once the distribution of coefficients is known, sets of coefficients can be

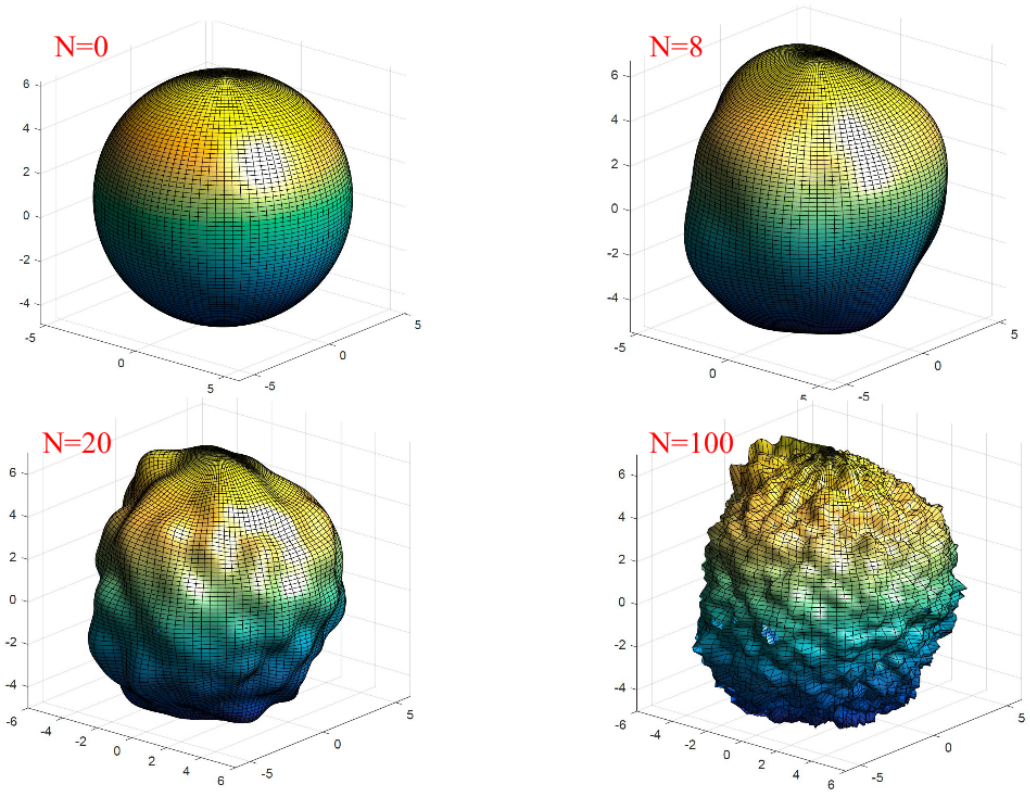

Figure 1: Particle representations with maximum degrees N=0, 8, 20 and 100. The coefficients $\{a_n^m\}$ and $\{b_n^m\}$ have been generated from uniform distributions

generated easily, allowing the simulation of a sample which is statistically identical to the experimental one.

Fig. 1 shows four representations obtained by truncating the expansion at N=0, 8, 20 and 100. Here the coefficients $\{a_n^m\}$ and $\{b_n^m\}$ have been obtained from a uniform distribution in the interval [-0.2, 0.8]. As N increases, the particle shape becomes more and more refined. The high-degree terms of the expansion are mainly responsible for microscopic details of the shape, e.g., the surface roughness.

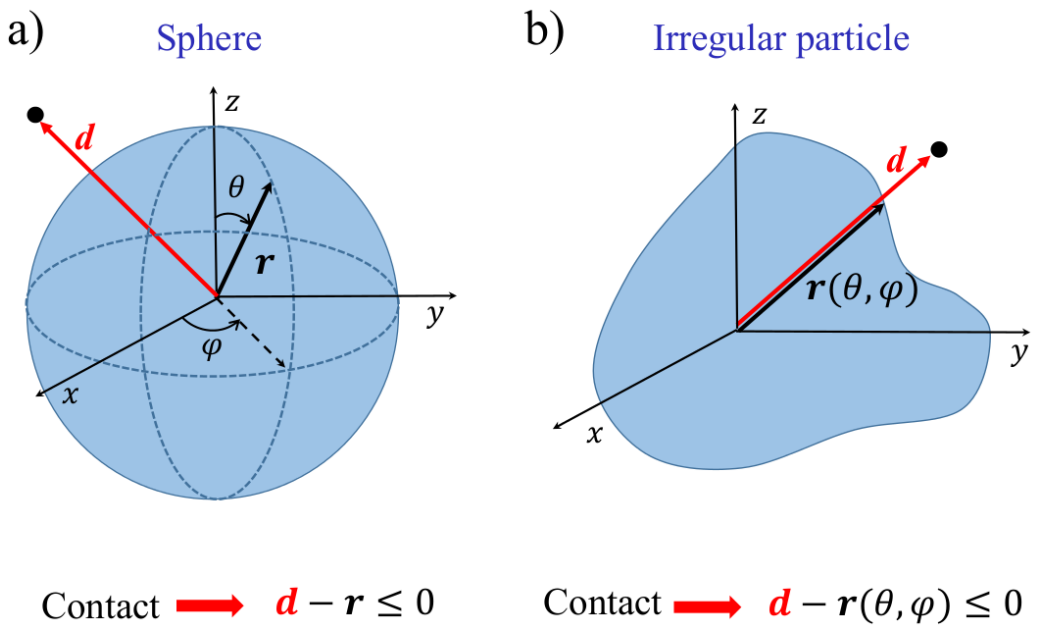

Figure 2: a) Contact detection between one single point and a sphere; b) Contact detection between a point and a particle of any 'star-like' shape. In this case a mathematical description of the shape is needed, i.e., $r = r(\theta, \varphi)$

3. Incorporation of spherical harmonics into DEM

3.1. Contact detection between arbitrary shapes

Contact detection between one single point and a sphere involves calculating the distance d between the point and the sphere's centre. Contact implies the function $d - r \leq 0$, where r is the sphere radius. A touching contact corresponds to $d = r$. The same idea can be generalised to particles of any shape as $d - r(\theta, \varphi) \leq 0$, where θ and φ are the polar angles as shown in Fig. 2. In this case we need a mathematical description of the shape where the radius $r(\theta, \varphi)$ changes as a function of θ and φ, namely the spherical harmonic representation of particle shape introduced in Section 2.

Spherical harmonics have the major benefit of providing not only one but a set of mathematical approximations of a particle's shape, which become increasingly refined as the degree of the expansion increases. This inherent property of spherical harmonics is well-suited to a multi-level representation, raising the question of why spherical harmonics have not previously been used for contact detection in DEM. The reason is illustrated in Fig. 3. The standard spherical harmonic representation of a particle does not require the shape obtained from an expansion to degree N to bound the shape obtained from a higher expansion to degree $N + j$. Thus, even though the spherical representation (N=0) of an irregularly shaped particle may have no inter-particle contacts, there is no assurance that a contact would not appear at N=5, for example. The resolution of this problem, so that low-degree expansions bound higher-degree expansions as required for a hierarchical contact detection scheme, is described in Section 3.2.

Instead of a single point, contact detection for two potentially contacting, non-spherical particles requires discretisation of one of the particles into many nodes, i.e., discrete function representation (DFR) [36–38]. Few nodes are needed when N is low and the surface is smooth; a higher density of nodes is needed when N is large and the surface texture needs to be described. Discretisation of a particle's surface is required only in the vicinity of potential contacts rather than for the entire particle which reduces the computational cost. A remaining issue, however, is the identification of a suitable discretisation method: if standard polar coordinates were used, the density of nodes would be highly non-uniform and divergent at the poles. The method adopted for this study to avoid this problem is described in

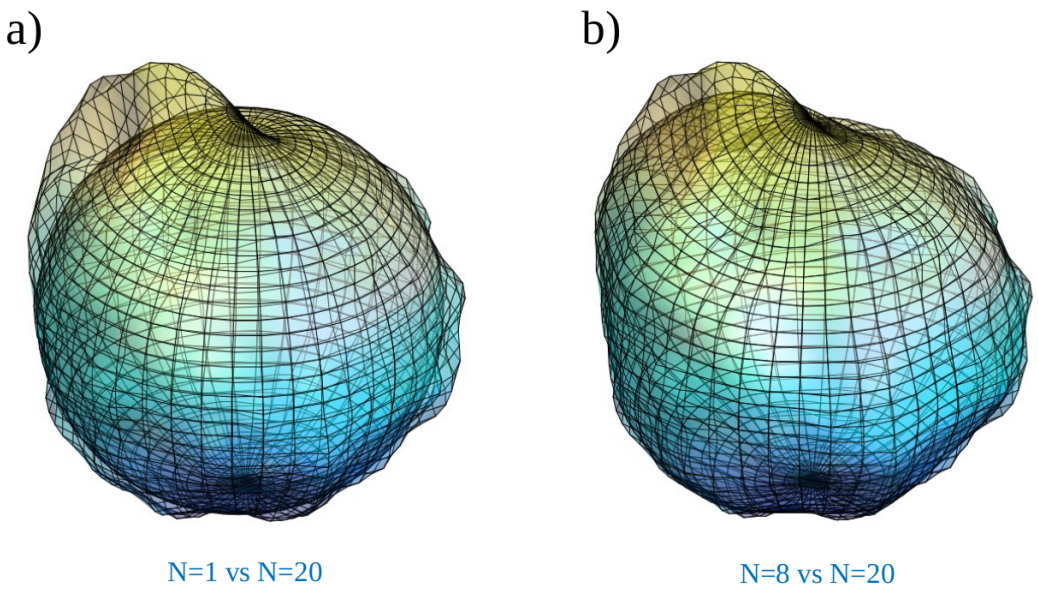

Figure 3: Comparison between the spherical harmonic expansions to a) N=1 and N=20; b) N=8 and N=20. The low-degree expansions N=1 and N=8 do not bound the higher-degree expansion to N=20

Section 3.3.

3.2. Adaptation for hierarchical contact detection

If N is the maximum degree of the expansion, we assume that the representation at degree N is the one which has the correct particle volume and shape. Evidently $L \leq N + 1$ particle representations can be generated, meaning that $\{q_1, q_2, \ldots, q_L\}$ intermediate values are selected from N with $q_L = N$. For example, if N=20 and L=3, we can choose q_1=0, q_2=8, q_3=20, the first representation being the sphere. To ensure that low-degree expansions bound higher-degree expansions, we multiply the expansion to degree $K = q_i$ by an extra coefficient, S_K, to obtain the adapted hierarchical

representation of the particle

$$r^{S}_{SH}(K,\theta,\varphi) = S_K \sum_{n=0}^{K} \sum_{m=-n}^{n} c_n^m Y_n^m(\theta,\varphi) = S_K\, r_{SH}(K,\theta,\varphi) \qquad (5)$$

where $S_{q_L} = 1$, $S_K = \prod_{j=1}^{L-i} v_{q_{L-j}}$, $v_{q_j} = \max\left\{\frac{r_{SH}(q_{j+1},\theta,\varphi)}{r_{SH}(q_j,\theta,\varphi)}\right\}$ is the maximum of the ratio between the two particle representations q_{j+1} and q_j. The coefficient S_K is a scaling factor that changes only the size of the particle representation, leaving all the other properties of the spherical harmonic expansion unchanged. Calculating the v_{q_j} terms is a straightforward procedure as the shape expanded to degree N is usually defined on a grid of points; therefore the expansion to N entails the calculation of $L-1$ additional coefficients $\{v_{q_1}, v_{q_2}, ..., v_{q_{L-1}}\}$. Eq. (5) is easily demonstrated from the recursive relation

$$\begin{aligned} r_{SH}(q_L,\theta,\varphi) \le v_{q_{L-1}}\, r_{SH}(q_{L-1},\theta,\varphi) \le v_{q_{L-1}}\, v_{q_{L-2}}\, r_{SH}(q_{L-2},\theta,\varphi) \le \ldots \\ \le v_{q_{L-1}}\, v_{q_{L-2}}\, \ldots v_{q_1}\, r_{SH}(q_1,\theta,\varphi) \end{aligned} \qquad (6)$$

The multiplication of the representation to degree K by S_K has a '*shrinking*' effect, when representation are compared from the lowest to the highest degree, as shown in Fig. 4. The rate of change of represented volumes slows as N becomes large (compare Fig. 4c with Fig. 4d). The change of volume depends on the number of representation levels L: the larger L is, the larger the cumulative change. Hence the 'all-level' representation with $L = N + 1$ shown in Fig. 4 is a worst-case scenario, while, in any practical implementation, $L < N$ will be used. Using fewer representation levels would have a less pronounced effect.

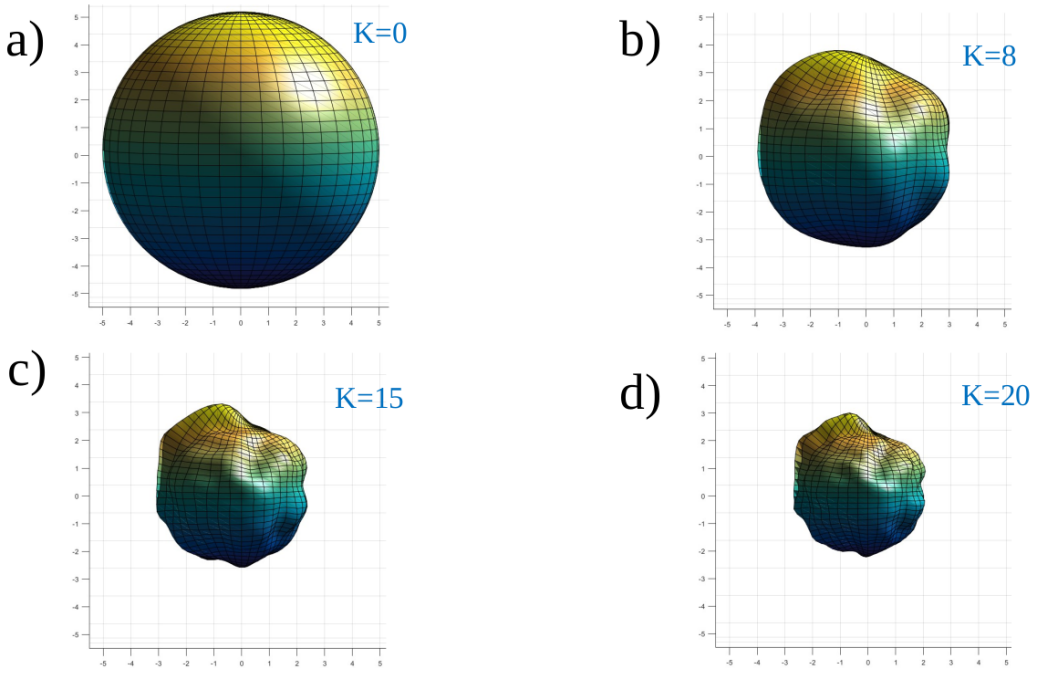

Figure 4: The effect of multiplying the representation to degree K by the scaling factor S_K when all degrees 0 to N are separately considered in the hierarchical representation. It ensures that the representation at degree K bounds the representation at $K + j$

3.3. Uniform density of nodes in discretisation

Consider initially the problem of uniformly distributing points on the surface of a sphere with radius r. One way to achieve this is to fix the distance between neighbouring points as $d_p = \frac{2\pi r}{N_p}$, with N_p being the number of points on the equator of the sphere. This also fixes the minimum angular distance between points $\Delta\theta = 2\pi/N_p$. Since $l(\theta) = 2\pi r \sin\theta$ is the θ-dependent length of each parallel, a number of points

$$n_p(\theta) = \frac{l(\theta)}{d_p} = N_p \sin\theta \tag{7}$$

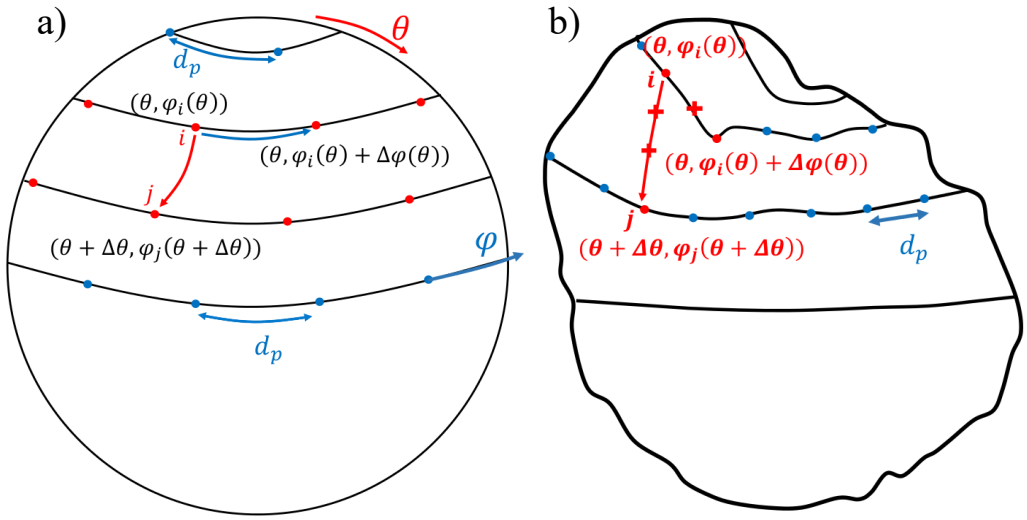

Figure 5: a) Uniform distribution of points on the surface of a sphere. The distance between neighbouring points is fixed as $d_p = \frac{2\pi r}{N_p}$, with N_p the number of points on the equator of the sphere. $n_p(\theta)$ points are assigned to each parallel, corresponding to the possible values $\varphi_i(\theta)$ of φ with $i = 1, \ldots, n_p(\theta)$. b) Uniform distribution of points on the surface of a non-spherical particle. Additional points (red '+') are added at high surface gradients, where $|r(\theta + \Delta\theta, \varphi + \Delta\varphi) - r(\theta, \varphi)| > d_p$

are assigned to each parallel, separated by angular distances $\Delta\varphi(\theta) = 2\pi/n_p(\theta)$. Once θ has been fixed, the possible values of φ are $\varphi_i(\theta) = \frac{2\pi}{n_p(\theta)} i$ with $i = 1, \ldots, n_p(\theta)$ (see Fig. 5a). This representation solves the problem of divergence at the poles. In fact, the smallest value of θ is $\Delta\theta = 2\pi/N_p$ so from Eq. (7) $n_p(\Delta\theta) = N_p \sin(\Delta\theta) \sim N_p \Delta\theta = 2\pi$.

This uniform discretisation procedure allows nodes to be uniformly distributed on the surface of a sphere [39]. However, in the case of non-spherical particles, regions with high surface gradients, where $|r(\theta + \Delta\theta, \varphi + \Delta\varphi) - r(\theta, \varphi)| > d_p$, must be taken into account. This is done by firstly

checking the distance between neighbouring points on the same parallel (θ fixed) of the uniform discretisation and then dividing by d_p, namely $\mathrm{NINT}(|r(\theta, \varphi_i(\theta) + \Delta\varphi(\theta)) - r(\theta, \varphi_i(\theta))|/d_p) = p$, where NINT stands for 'nearest integer'. p points are then added to the uniform representation, calculating $\{r(\theta, \varphi_i(\theta) + d\varphi_p), r(\theta, \varphi_i(\theta) + 2d\varphi_p), \ldots, r(\theta, \varphi_i(\theta) + pd\varphi_p)\}$ where $d\varphi_p = \Delta\varphi(\theta)/p$ (see the '+' symbols indicated in Fig. 5b). The same procedure is followed for neighbouring points on different parallels by changing θ. However, discretised values of φ on different parallels can be different, i.e., $\varphi_i(\theta) \neq \varphi_j(\theta+\Delta\theta)$, $\forall j \in \{1, \ldots, n_p(\theta+\Delta\theta)\}$ (see Fig. 5a). Therefore, we need to find the value $\varphi_j(\theta+\Delta\theta)$ closest to $\varphi_i(\theta)$, namely $\min(|\varphi_i(\theta)-\varphi_j(\theta+\Delta\theta)|)$. Considering that $\varphi_i(\theta) = i\frac{2\pi}{n_p(\theta)}$ and $\varphi_j(\theta+\Delta\theta) = j\frac{2\pi}{n_p(\theta+\Delta\theta)}$, we get the simple relation

$$j = \mathrm{NINT}\left(i\frac{n_p(\theta + \Delta\theta)}{n_p(\theta)}\right) \tag{8}$$

We therefore calculate $\mathrm{NINT}(|r(\theta + \Delta\theta, \varphi_j(\theta + \Delta\theta)) - r(\theta, \varphi_i(\theta))|/d_p) = p$, and add the points $\{r(\theta+d\theta_p, \varphi_i(\theta)+d\varphi_p), r(\theta+2d\theta_p, \varphi_i(\theta)+2d\varphi_p), \ldots, r(\theta+pd\theta_p, \varphi_i(\theta) + pd\varphi_p)\}$, where $d\theta_p = \Delta\theta/p$ and $d\varphi_p = (\varphi_j(\theta + \Delta\theta) - \varphi_i(\theta))/p$. In this way the representation shown in Fig. 6 is obtained.

4. Case study: two-level representation of two interacting particles

A proof-of-concept code was developed for two interacting particles, represented at two hierarchical levels of detail, i.e. $L = 2$ with $q_2 = N = 20$ and $q_1 = 8$. These two representations have been arbitrarily chosen for the purpose of this demonstration whose scope was not to test the dynamics but to check that this new method is viable and can be easily implemented in a standard rigid-body dynamics scheme.

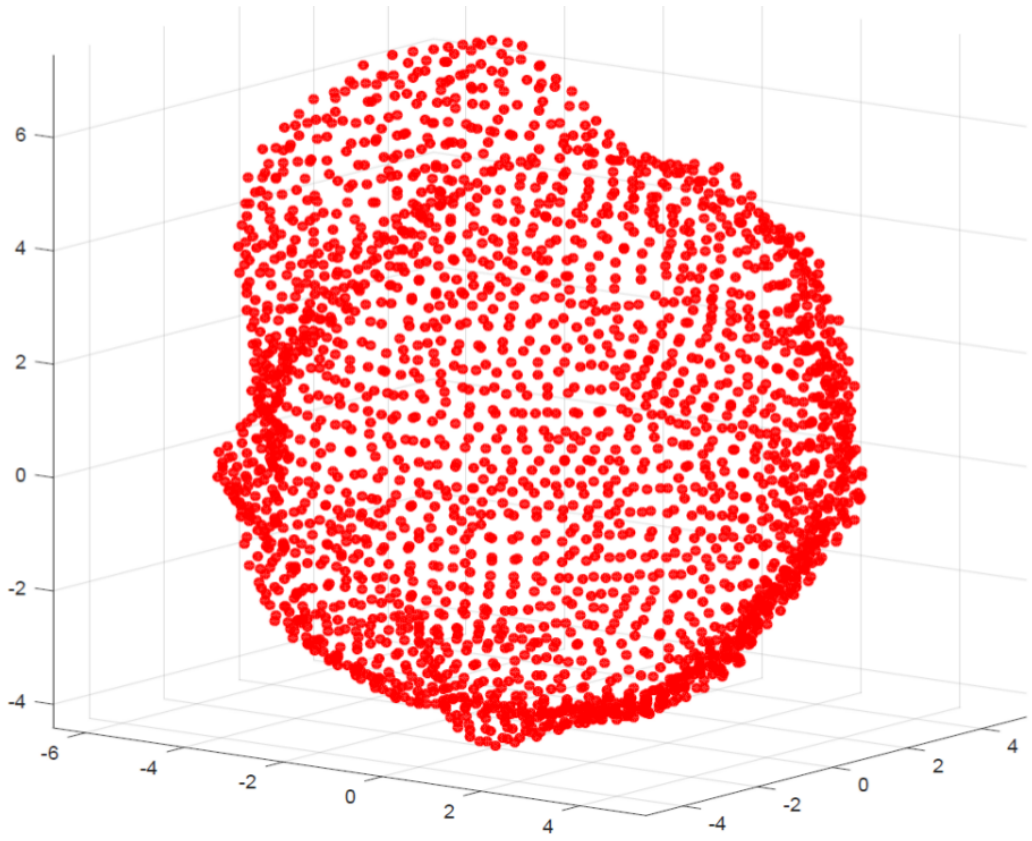

Figure 6: Uniform distribution of points on the surface of a non-spherical particle, obtained through the described algorithm

To initialise the system, two sets of coefficients were generated from a uniform distribution: $\{a^m_{n,1}, b^m_{n,1}\}$ for particle 1 and $\{a^m_{n,2}, b^m_{n,2}\}$ for particle 2. From Eq. (4), four representations $r_{SH,i}(q_j, \theta, \varphi)$ were obtained with particle indices i=1, 2 and representation indices j=1, 2 (q_2=20 and q_1=8). The representations were discretised uniformly as explained in Section 3.3, and coefficients $S_{8,i}$ were calculated (Eq. (5)), ensuring that $r_{SH,i}(20, \theta, \varphi) \leq S_{8,i}\, r_{SH,i}(8, \theta, \varphi) = r^S_{SH,i}(8, \theta, \varphi)$. Here we reserve the word 'nodes' to refer to those points which discretise $r^S_{SH,i}(8, \theta, \varphi)$, and 'asperities' for the points

discretising $r_{SH,i}(20, \theta, \varphi)$. On Fig. 7, the former are shown as large blue circular markers of which there are m_1^n=164 nodes for particle 1 and m_2^n=155 nodes for particle 2; the latter as small red circular markers with m_1^a=1800 and m_2^a=1900 asperities for particles 1 and 2, respectively. Fig. 7 shows that $r_{SH,i}^S(8, \theta, \varphi)$ does not describe the fine features of the particle: it is a bounding shape to be used for contact detection. Hence the numbers of nodes m_i^n are more than one order of magnitude smaller than the numbers of asperities m_i^a needed to accurately describe the particles' morphology [57]. The moments of inertia $\boldsymbol{I}_i$ were calculated in advance for the N=20 representations of these two particles, assuming a uniform mass density of the objects. For this proof-of-concept, the m_i^n node positions, coefficients $\{a_{n,1}^m, b_{n,1}^m\}$, $\{a_{n,2}^m, b_{n,2}^m\}$ and $S_{8,i}$ were stored at the start of the simulation.

Several important differences between this two-particle demonstration and a future implementation in a large-scale code, e.g. LAMMPS (see Section 6) should be emphasised:

- In practice, one would always choose to begin with the representation to degree q_1=0, rather than q_1=8 in this instance, to take advantage of the computational efficiency afforded by bounding spheres. In that case, the first stage of contact detection (sphere–sphere) would proceed as in a conventional sphere-based DEM code, i.e., neither bounding sphere would be discretised. This would substantially reduce the number of potential interparticle contacts before progressing to $q_j > 0$ which is more computationally costly.

- In this test case, both particles were discretised in order to calculate the interparticle force using a Lennard-Jones molecular interaction. In

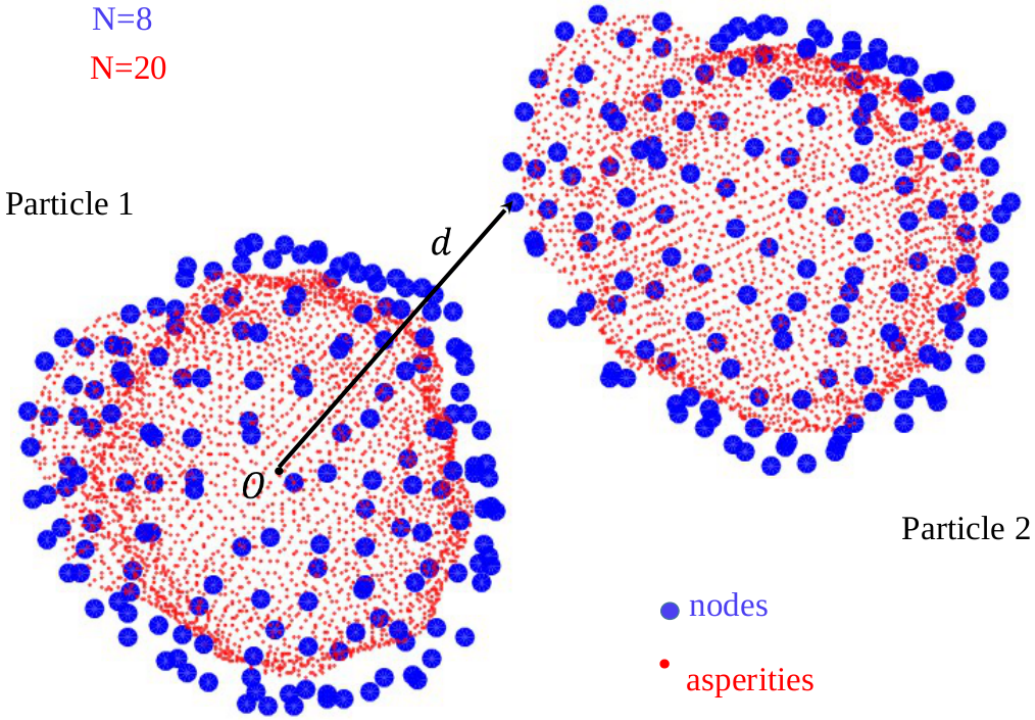

Figure 7: Two-level representation of two approaching particles $r^S_{SH,i}(8,\theta,\varphi)$ and $r_{SH,i}(20,\theta,\varphi)$, with degrees $q_1 = 8$ and $q_2 = N = 20$, respectively. Blue nodes are used to discretise $r^S_{SH,i}(8,\theta,\varphi)$; red asperities discretise $r_{SH,i}(20,\theta,\varphi)$

DEM, it is usual to adopt a contact law based on Hookean or Hertzian mechanics, in which case only one of two contacting particles would require discretisation while the other would remain as an analytical expression. Furthermore, discretisation is only required in the vicinity of a possible contact. If starting at q_1=0, nodes would only be required wherever bounding spheres intersect.

Contact detection employing one discretised particle representation and one analytical representation has previously been discussed in the literature [36,

39]. In order to check whether any of the m_2^n nodes of particle 2 overlap with particle 1, the nodes are parsed to search for overlaps as $d - r_{SH,1}^S(8, \Theta_1, \Phi_1) \leq 0$ where d is the length of the line segment joining the origin of particle 1 and a node of particle 2 (see Fig. 7) and Θ_1 and Φ_1 are the polar angles of the line segment in particle 1's reference frame.

In principle, it would be equivalent to reverse the roles of particles 1 and 2, i.e., use the m_1^n nodes of particle 1 and the analytical representation of particle 2. However, in practice, asperities would not be generated at identical positions if 1 and 2's roles were reversed so there would be a small discrepancy between the computed forces. This disparity would be reduced by increasing the density of nodes describing the discretised surface.

If an overlap is found, the discretised particle's representation is refined around the overlapping nodes. To refine to N=20 for this demonstration, the representations $r_{SH,i}(20, \Theta_i \pm \Delta\Theta, \Phi_i \pm \Delta\Phi)$ were used to generate asperities 'on the fly' solely around the Θ_i and Φ_i angles, where Θ_2 and Φ_2 are the polar angles of the line segment joining the origin of particle 2 and the overlapping node of particle 2. Here $\Delta\Theta = |\frac{\Theta_{i+1} - \Theta_i}{2}|$ and $\Delta\Phi = |\frac{\Phi_{i+1} - \Phi_i}{2}|$ stand for the angular half-distance between the overlapping node and the adjacent nodes. The asperities are shown on Fig. 7 for the entirety of both particles rather than for a small region of one particle. Ultimately, once the asperities have been generated where required, the net force is calculated as the sum of the forces from each individual asperity.

It is noted that DEM contact laws for non-spherical particles are lacking at present; additional research in this area is ongoing which will complement the development presented in this paper. These contact laws should involve

the calculation of the normal to the analytical representation, and estimation of the contact width or overlap volume [58]. To calculate the force at the single-asperity level, it would be necessary to assign a portion of the total overlapping volume to each asperity [58].

From forces on the asperities, the torque $\boldsymbol{\tau}_i$ is calculated for each particle and the angular momentum $\boldsymbol{L}_i$ is updated. However, the moment of inertia, $\boldsymbol{I}_i$, is time-varying in a global coordinate system. Thus, a suitable body particle-fixed coordinate system is usually introduced, where the inertia tensor $\boldsymbol{I}_i^B$ contains only non-zero entries on its diagonal, referred to as the principal moments of inertia. By using the rotation matrix, $\boldsymbol{R}_i$, transforming vectors between the two reference frames, the angular velocity, $\boldsymbol{\omega}_i$, can be calculated as

$$\boldsymbol{\omega}_i = \boldsymbol{R}_i \boldsymbol{\omega}_i^B = \boldsymbol{R}_i (\boldsymbol{I}_i^B)^{-1} \boldsymbol{R}_i^T \boldsymbol{L}_i \tag{9}$$

where $\boldsymbol{R}_i^T$ is the transpose of the $\boldsymbol{R}_i$ matrix and the relations $\boldsymbol{\omega}_i^B = (\boldsymbol{I}_i^B)^{-1} \boldsymbol{L}_i^B$, $\boldsymbol{L}_i^B = \boldsymbol{R}_i^T \boldsymbol{L}_i$ are applied. The rotation matrix $\boldsymbol{R}_i$ is updated at each time-step by using the standard quaternion approach [59]. The particle rotations and orientation are tracked during the simulation using standard algorithms for rigid-body dynamics.

Fig. 8 shows a snapshot of the two-particle simulation once the particles had come into contact. The small red markers on Fig. 8 denote the asperities generated once the overlap had been detected using the procedure outlined above.

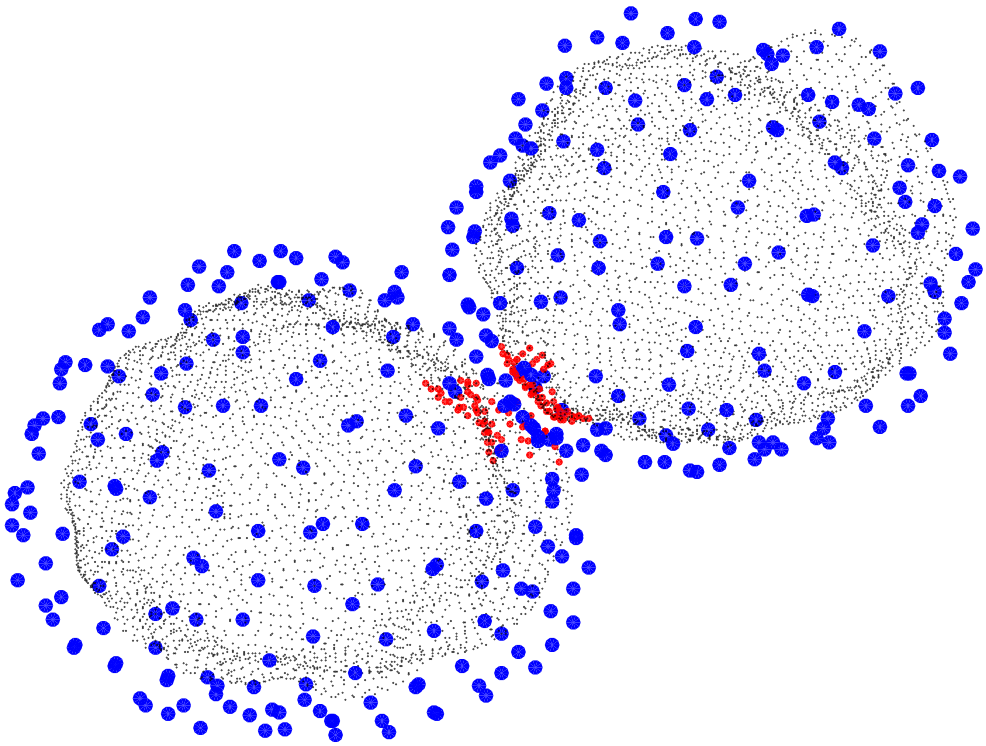

Figure 8: Snapshot of the simulation. The red dots indicate the asperities around overlapping nodes. The smaller black dots indicate the precise morphologies of both particles

5. Extension to include particle abrasion by chipping

The loss of particle mass is due to three mechanisms: frictional abrasion, chipping, and fragmentation. Frictional abrasion during contact sliding smooths the faces and leads to the formation of flat or cylindrical particles [60]. Chipping occurs at larger energies, when collisions form shallow cracks that lead to the production of much smaller fragments [61]. Chipping preferentially attacks the edges and corners of the grains, leading to rounding and the evolution of particles towards a spherical shape [14, 61]. At sufficiently large collision energies, fractures propagate throughout a particle and lead

to its breakup by fragmentation [62, 63].

The spherical harmonic framework, which includes a hierarchy of related particle shapes, could potentially be applied to capture abrasion of a particle's surface by chipping. If the particle is assumed to be bombarded isotropically by a field of large, rough objects, this would lead to a smoothening and loss of roughness. In such a case, the normal erosion rate, ds/dt, at which a region of the surface near a point P erodes depends on the curvature [13]:

$$\frac{ds}{dt} = v(1 + AH + BK) \tag{10}$$

where v is a constant, and H and K are the mean and Gaussian curvatures. The parameters A and B depend on the size of impacting particles, representing their average (or effective) radius and area, respectively. As expected, the erosion rate is highest where the curvature is greatest and angular regions erode much faster than flat ones [64].

By considering the particle shape at time t, $r(\theta, \varphi, t) = a(t)(1+\epsilon(\theta, \varphi, t))$ as a perturbed sphere of radius $a(t)$ and expanding ϵ as a sum of spherical harmonics,

$$\epsilon(\theta, \varphi, t) = \sum_{n=0}^{\infty} \sum_{m=-n}^{n} \epsilon_n^m(t) Y_n^m(\theta, \varphi) \tag{11}$$

it can be shown that higher harmonics decay with time much more rapidly than the lower ones [13] and the ellipsoidal one, $n = 2$, lasts the longest. These mathematical considerations, together with recent experimental results [12], strongly support the idea that higher harmonics, corresponding to the surface texture, are the first to be eroded, while ellipsoidal shapes, found in abundance in nature, take much longer to become spherical, i.e., the sphere is the equilibrium shape [13]. Therefore, representing the abrasion process

through the sequential removal of the highest spherical harmonics is an attractive idea. During abrasion, mass is lost and it must be ensured that the high-degree spherical harmonic expansion, representing the original shape, bounds the expansion at any lower degree: the abraded shape. We propose a strategy similar to the one in Eq. (5), multiplying the expansion to degree K by a scaling factor, s_K,

$$r^s_{SH}(K,\theta,\varphi) = s_K \sum_{n=0}^{K} \sum_{m=-n}^{n} c_n^m Y_n^m(\theta,\varphi) = s_K \; r_{SH}(K,\theta,\varphi) \qquad (12)$$

where N is the maximum degree, $s_N = 1$, $s_K = \prod_{j=1}^{N-K} 1/u_{N-j}$ and $u_i = \max\left\{\frac{r_{SH}(i,\theta,\varphi)}{r_{SH}(i+1,\theta,\varphi)}\right\}$. Fig. 9 shows a set of four expansions with $N = 40$ and K=40, 30, 10, 2 obtained by eliminating higher harmonic terms from the expansion and multiplying by the scaling factor s_K. The removal of the highest harmonics leaves the overall shape unchanged (compare K=40 with K=30), affecting mostly the particle texture and roughness. However, when the expansion is limited to the lowest harmonics, the particle shape is strongly affected, reducing eventually to an ellipsoid.

It has been demonstrated that the mass of particles (M) undergoing a wearing process decreases exponentially with time [12] or distance (x) travelled [65] according to

$$M = M_0 e^{-kx} \qquad (13)$$

where M_0 is initial mass and k is an empirically determined coefficient which depends on the material properties and wearing conditions. Eq. (13) is quite general and has been proven in many different experimental situations [66, 67]: it states that while the rate of mass loss due to abrasion is very rapid initially, it slows down with the distance travelled. From Eq. (12), we can

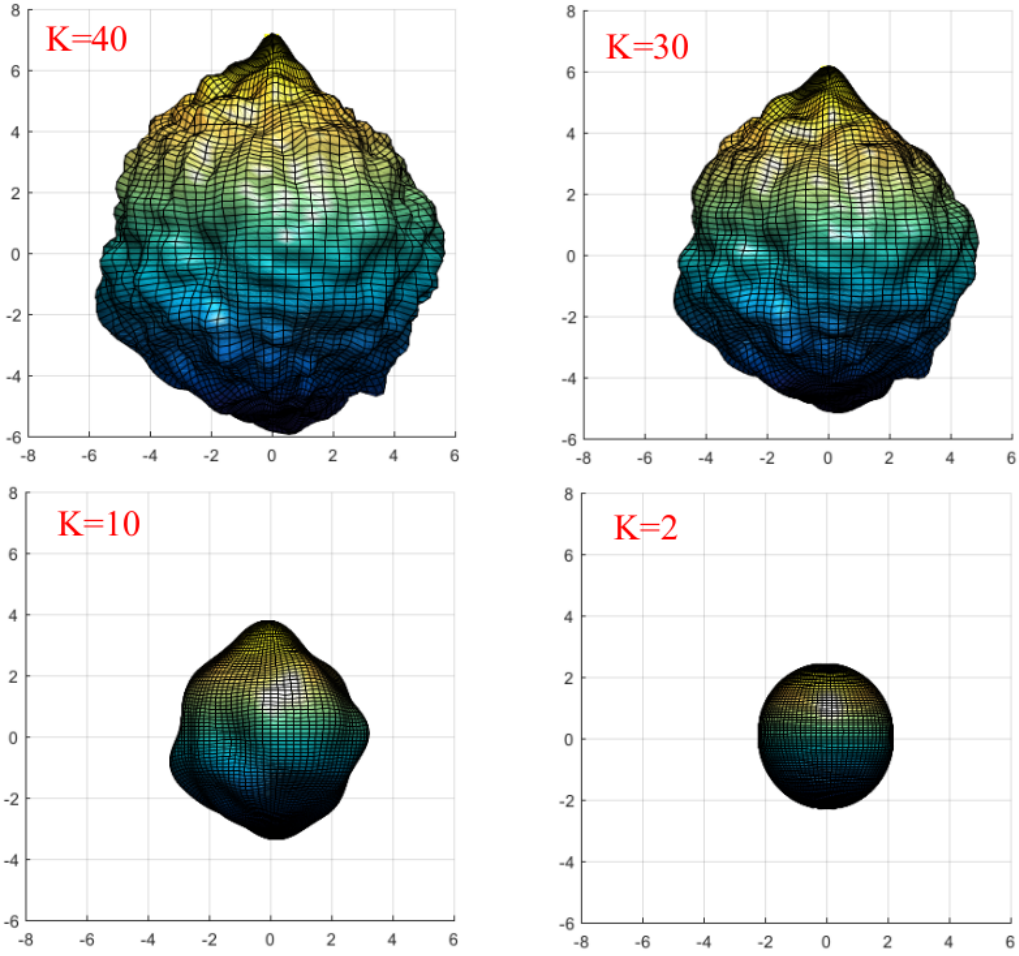

Figure 9: Four expansions for K=40, 30, 10 and 2 obtained by eliminating higher harmonic terms from the expansion and multiplying by the scaling factor s_K

write the abraded shapes to degree K in spherical coordinates and therefore calculate their K-dependent volumes as:

$$V_K = \int_0^{\pi} \int_0^{2\pi} \int_0^{r(K,\theta,\varphi)} \rho^2 \sin(\theta) d\theta d\varphi d\rho = \int_0^{\pi} \sin(\theta) d\theta \int_0^{2\pi} \frac{r^3(K,\theta,\varphi)}{3} d\varphi \tag{14}$$

where $dv = \rho^2 \sin(\theta) d\theta d\varphi d\rho$ is the volume element and $r(K,\theta,\varphi)$ is a shorter

notation to indicate $r^s_{SH}(K,\theta,\varphi)$ in Eq. (12). Fig. 10 shows that the particle volume is a decreasing function of the degree. If the 'mass-loss' function is known for a particular process and the density of the particle is constant throughout, the distance x travelled can be estimated from the particle mass M by inverting Eq. (13).

As high harmonics only change the texture of a particle's surface [12], we would expect a small volume change at a high degree, as reported in literature [51]. However, to ensure that the expansion at higher degrees bound those at lower degrees, we 'shrink' the shape using the coefficients s_K. The relative volume change $V^r_K = (V_K - V_{K-1})/V_{ave}$ can be defined where $V_{ave} = \frac{V_K+V_{K-1}}{2}$ is the average volume. V^r_K is plotted as a function of the degree in Fig. 10b. V^r_K shows minor variations at high harmonics, with a growing trend toward low harmonics, as expected.

The change of volume determines the quantity of fines produced. The change of particle surface area is also important as this affects, for example, the particle's effectiveness as a catalyst (noting that particles are taken to be solid rather than porous which would usually be the case). The area can be estimated by integrating the differential surface area element $dA = |\frac{d\vec{r}}{d\theta} \times \frac{d\vec{r}}{d\varphi}| d\theta d\varphi$, representing the area of each small 'tile' in Fig. 9, over θ and φ. $\vec{r}$ is the vector with norm $r(K,\theta,\varphi)$ and direction given by (θ,φ). It can be shown that $dA = r\left(r^2_\varphi + r^2_\theta \sin^2\theta + r^2 \sin^2\theta\right)^{1/2} d\theta d\varphi$ with $r_\varphi = \frac{d\vec{r}}{d\varphi}$, $r_\theta = \frac{d\vec{r}}{d\theta}$, so that the surface area, A_K, to degree K is

$$A_K = \int_0^{\pi} \int_0^{2\pi} r^2(N,\theta,\varphi)\left(r^2_\varphi + r^2_\theta \sin^2\theta + r^2(N,\theta,\varphi)\sin^2\theta\right)^{1/2} d\theta d\varphi \quad (15)$$

The behaviour of A_K as a function of degree is reported in Fig. 11a. As for the volume V_K, the decrease of area is due to the shrinking of the shape, so

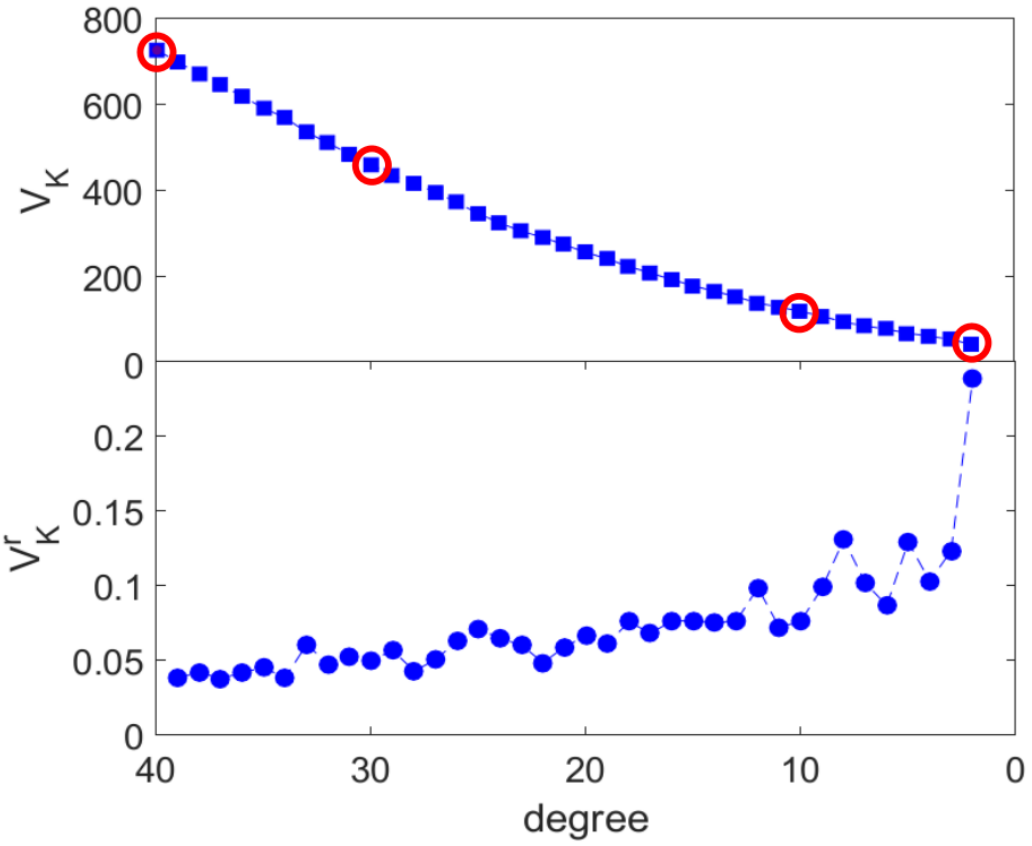

Figure 10: Particle volume V_K and relative volume change V_K^r as a function of the degree. Red circles refer to the expansions shown in Fig. 9

the relative area change, $A_K^r = (A_K - A_{K-1})/A_{ave}$, is also shown (Fig. 11b), where $A_{ave} = \frac{A_K + A_{K-1}}{2}$ is the average area. A_K^r changes more significantly as the degree is reduced, particularly at lower degrees.

6. Discussion and proposed implementation

Sections 3–5 establish the fundamental principles of a new method for the simulation of abradable, irregularly shaped particles. Next this will be

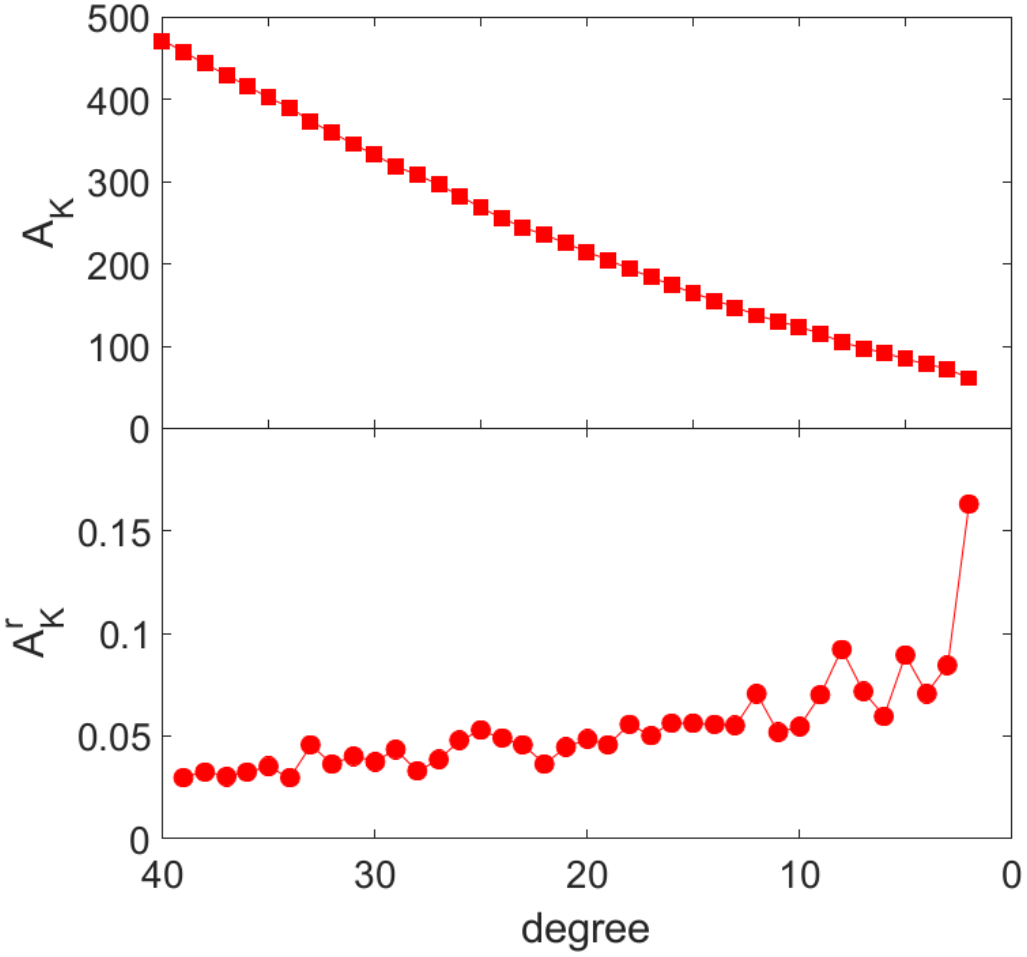

Figure 11: Particle area A_K and relative area change A^r_K as a function of the degree

implemented in a suitable code, e.g. LAMMPS [50]. Through a suitable choice of representations, particles will be simulated at multiple levels of resolution, beginning with bounding spheres (N=0) before progressively refining the shapes around potential contacts to ultimately achieve the desired level of shape fidelity at the interparticle contacts. The fidelity can change temporally, e.g., particles may be simulated less accurately during sample

preparation than subsequently. The fidelity could also depend on the location of a particle within the simulation domain, i.e., more refined particles (higher N) could be used at locations within the domain which are deemed to be of particular interest. This raises the possibility of emulating the common practice in finite element analyses of simulating regions within the domain with greater refinement (smaller elements) than others, e.g., at the boundary of the domain. The commonly used sphere-based contact detection algorithm can be retained for the bounding spheres. The intention is to carry out the hierarchical refinement of the particles within the contact law (e.g., 'pair style' in LAMMPS).

There is, of course, considerable potential to improve the computational performance of this method compared to the two-particle demonstration. For example, no information about computed overlaps or nodes is carried forward to the following time step which has the potential to reduce the computational effort substantially. In addition, a high density of nodes has been used for discretisation in this two-particle demonstration. An open question, which will be investigated as part of the future work on developing this method, is the optimal density of nodes to strike an appropriate balance between efficiency of contact resolution and accuracy. This density of nodes should change between representations: the higher the degree, the greater the density of nodes needed to describe shape details and surface texture. Reducing the number of nodes without significantly degrading the accuracy could greatly reduce the computational cost.

A physical rationale, e.g., Archard's law, will be imposed for particle

abrasion:

$$Q = W F_n l_t \tag{16}$$

where Q is the volume of material removed, W is a constant, F_n the normal load and l_t the sliding distance. Since F_n and l_t are known quantities for each pair of interparticle contacts in DEM, Q can be calculated once W has been calibrated appropriately using experimental data. Therefore, from the number of collisions, it will be possible to estimate the loss of volume and then the particle shrinkage to a lower degree K; this latter representation will become the new reference shape for the hierarchical representation. More precisely, each particle representation, $r^S_{SH}(a, h, \theta, \varphi)$, will be characterised by two parameters, a and h, representing 'abrasion' and 'hierarchical' indices, respectively. The values of a and h constitute a two-dimensional array, as each abraded shape will correspond to a number of possible representations.

7. Conclusions

In this paper, we have presented the essential foundation for incorporating spherical harmonics into a DEM simulation for the purpose of simulating the dynamics of realistically shaped particles. We have shown that spherical harmonics can be used not only for the representation of particles via the calculation of the coefficients, but could be practically integrated into a DEM code and even benefit contact detection between non-spherical particles through the use of suitable scaling factors. A detailed description of particle shape is computed only at interparticle contacts which reduces the computational cost, while the use of the scaling factors enables a hierarchical contact detection approach. This paves the way for the widespread use of spherical

harmonics in DEM simulations. The feasibility of a spherical harmonic-based DEM simulation has been shown for only two particles, where a simple algorithm for the generation of asperities 'on the fly' is added to a classical rigid-body dynamics scheme.

Additionally, based on mathematical considerations and experimental evidence, it has been shown that abrasion can be simulated by the sequential removal of high harmonics from the spherical harmonic expansion. This abrasion can be related to a microscopic wearing law, such as Archard's law, and incorporated into the hierarchical particle simulation approach. Each abraded shape will be associated with a set of multi-level shape representations, i.e., spherical harmonic coefficients.

Potential improvements and future development will include the calculation of an *optimal* density of nodes, to reduce the computational cost without significantly degrading the accuracy.

Acknowledgement

This research was funded by the UK Engineering and Physical Sciences Research Council (EPSRC) grant EP/R005877/1. The authors thank Kevin Stratford (EPCC) and James Young (University of Edinburgh) for their feedback on a draft of this paper.

References

[1] T. Miyajima, K.-I. Yamamoto, M. Sugimoto, Effect of particle shape on packing properties during tapping, Adv. Powder Technol. 12 (1) (2001) 117–134.

[2] C. Zhou, J. Y. Ooi, Numerical investigation of progressive development of granular pile with spherical and non-spherical particles., Mech. Mater. 41 (6) (2009) 707–714.

[3] Z. Y. Zhou, R. P. Zou, D. Pinson, A. B. Yu, Angle of repose and stress distribution of sandpiles formed with ellipsoidal particles, Granul. Matter 16 (6) (2014) 695–709.

[4] T. Pöschel, V. Buchholtz, Complex flow of granular material in a rotating cylinder., Chaos Soliton. Fract. 5 (10) (1995) 1901–1905.

[5] G. G. W. Mustoe, M. Miyata, Material flow analyses of noncircular-shaped granular media using discrete element methods., J. Eng. Mech. 127 (10) (2001) 1017–1026.

[6] S. J. Roskilly, E. A. Colbourn, O. Alli, D. Williams, K. A. Paul, E. H. Welfare, P. A. Trusty, Investigating the effect of shape on particle segregation using a Monte Carlo simulation, Powder Technol 203 (2) (2010) 211–222.

[7] G. G. Pereira, P. W. Cleary, Segregation due to particle shape of a granular mixture in a slowly rotating tumbler, Granul. Matter 19 (2017) 23–1–23–12.

[8] P. W. Cleary, M. L. Sawley, DEM modelling of industrial granular flows: 3D case studies and the effect of particle shape on hopper discharge, Appl. Math. Model 26 (2) (2002) 89–111.

[9] D. Höhner, S. Wirtz, V. Scherer, A numerical study on the influence

of particle shape on hopper discharge within the polyhedral and multi-sphere discrete element method, Powder Technol. 226 (2012) 16–28.

[10] E. Azéma, F. Radjai, F. Dubois, Packings of irregular polyhedral particles: strength, structure, and effects of angularity, Phys. Rev. E 87 (2013) 062203.

[11] B. Soltanbeigi, A. Podlozhnyuk, S.-A. Papanicolopulos, C. Kloss, S. Pirker, J. Y. Ooi, DEM study of mechanical characteristics of multi-spherical and superquadric particles at micro and macro scales, Powder Technol. 329 (2018) 288–303.

[12] I. Deiros Quintanilla, G. Combe, F. Emeriault, C. Voivret, J. Ferellec, X-ray CT analysis of the evolution of ballast grain morphology along a Micro-Deval test: key role of the asperity scale, Granul. Matter 21 (2019) 30–1–30–12.

[13] J. F. Bloore, The shape of pebbles, Math. Geol. 9 (1977) 113–122.

[14] G. Domokos, D. J. Jerolmack, A. Á. Sipos, Á. Török, How river rocks round: resolving the shape-size paradox, PLoS One 9 (2) (2014) e88657.

[15] G. Lu, J. R. Third, C. R. Müller, Discrete element models for non-spherical particle systems: From theoretical developments to applications, Chem. Eng. Sci. 127 (2015) 425–465.

[16] W. Zhong, A. Yu, X. Liu, Z. Tong, H. Zhang, DEM/CFD-DEM modelling of non-spherical particulate systems: Theoretical developments and applications, Powder Technol. 302 (2016) 108–152.

[17] T. D. Nguyen, S. J. Plimpton, Aspherical particle models for molecular dynamics simulation, Comput. Phys. Commun. 243 (2019) 12–24.

[18] C. M. Wensrich, A. Katterfeld, Rolling friction as a technique for modelling particle shape in DEM, Powder Technol. 217 (2012) 409–417.

[19] X. Huang, K. J. Hanley, C. O'Sullivan, C.-Y. Kwok, Implementation of rotational resistance models: A critical appraisal, Particuology 34 (2017) 14–23.

[20] X. Lin, T.-T. Ng, Contact detection algorithms for three-dimensional ellipsoids in discrete element modelling, Int. J. Numer. Anal. Methods Geomech. 19 (9) (1995) 653–659.

[21] J. R. Williams, A. P. Pentland, Superquadrics and modal dynamics for discrete elements in interactive design, Eng. Computation. 9 (2) (1992) 115–127.

[22] E. Seyedi Hosseininia, A. A. Mirghasemi, Numerical simulation of breakage of two-dimensional polygon-shaped particles using discrete element method., Powder Technol. 166 (2) (2006) 100–112.

[23] R. Hart, P. A. Cundall, J. Lemos, Formulation of a three-dimensional distinct element model – Part II. mechanical calculations for motion and interaction of a system composed of many polyhedral blocks., Int. J. Rock Mech. Min. Sci. Geomech. Abstr. 25 (3) (1988) 117–125.

[24] J. Ghaboussi, R. Barbosa, Three-dimensional discrete element method for granular materials, Int. J. Numer. Anal. Methods Geomech. 14 (7) (1990) 451–472.

[25] DEM Solutions Ltd., EDEM 2019 User Guide, https://www.edemsimulation.com/ (2019).

[26] Itasca Consulting Group, Inc., PFC 5.0 Documentation (2015).

[27] J. F. Favier, M. H. Abbaspour-Fard, M. Kremmer, A. O. Raji, Shape representation of axi-symmetrical, non-spherical particles in discrete element simulation using multi-element model particles, Eng. Computation. 16 (4) (1999) 467–480.

[28] M. Marigo, E. H. Stitt, Discrete element method (DEM) for industrial applications: Comments on calibration and validation for the modelling of cylindrical pellets, KONA Powder Part. Technol. J. 32 (2015) 236–252.

[29] H. Kruggel-Emden, S. Rickelt, S. Wirtz, V. Scherer, A study on the validity of the multi-sphere Discrete Element Method, Powder Technol. 188 (2008) 153–165.

[30] J. E. Andrade, K.-W. Lim, C. F. Avila, I. Vlahinić, Granular element method for computational particle mechanics., Comput. Methods Appl. Mech. Eng. 241–244 (2012) 262–274.

[31] G. T. Houlsby, Potential particles: a method for modelling non-circular particles in DEM, Comput. Geotech. 36 (6) (2009) 953–959.

[32] C. W. Boon, G. T. Houlsby, S. Utili, A new contact detection algorithm for three-dimensional non-spherical particles, Powder Technol. 248 (2013) 94–102.

[33] F. Alonso-Marroquín, Y. Wang, An efficient algorithm for granular dynamics simulations with complex-shaped objects, Granul. Matter 11 (5) (2009) 317–329.

[34] I. Vlahinić, E. Andò, G. Viggiani, J. E. Andrade, Towards a more accurate characterization of granular media: extracting quantitative descriptors from tomographic images, Granul. Matter 16 (2014) 9–21.

[35] D. Markauskas, R. Kačianauskas, A. Džiugys, R. Navakas, Investigation of adequacy of multi-sphere approximation of elliptical particles for DEM simulations, Granul. Matter 12 (2009) 107–123.

[36] C. Hogue, Shape representation and contact detection for discrete element simulations of arbitrary geometries, Eng. Computation. 15 (3) (1998) 374–390.

[37] J. R. Williams, R. O'Connor, A linear complexity intersection algorithm for discrete element simulation of arbitrary geometries, Eng. Computation. 12 (2) (1995) 185–201.

[38] J. R. Williams, R. O'Connor, Discrete element simulation and the contact problem, Arch. Comput. Method. E. 6 (4) (1999) 279–304.

[39] G. Lu, J. R. Third, C. R. Müller, Critical assessment of two approaches for evaluating contacts between super-quadric shaped particles in DEM simulations, Chem. Eng. Sci. 78 (2012) 226–235.

[40] A. Lekhal, K. P. Girard, M. A. Brown, S. Kiang, B. J. Glasser, J. G. Khinast, Impact of agitated drying on crystal morphology: KCl–water system, Powder Technol. 132 (2–3) (2003) 119–130.

603 [41] E. Kougoulos, C. E. Chadwick, M. D. Ticehurst, Impact of agitated
604 drying on the powder properties of an active pharmaceutical ingredient,
605 Powder Technol. 210 (3) (2011) 308–314.

606 [42] C. Hare, M. Ghadiri, R. Dennehy, Prediction of attrition in agitated
607 particle beds, Chem. Eng. Sci. 66 (20) (2011) 4757–4770.

608 [43] X. Hua, J. Curtis, Y. Guo, B. Hancock, W. Ketterhagen, C. Wassgren,
609 The internal loads, moments, and stresses in rod-like particles in a low-
610 speed, vertical axis mixer, Chem. Eng. Sci. 134 (2015) 581–598.

611 [44] K. J. Hanley, E. P. Byrne, K. Cronin, J. C. Oliveira, J. A. O'Mahony,
612 M. A. Fenelon, Effect of pneumatic conveying parameters on physical
613 quality characteristics of infant formula, J. Food Eng. 106 (3) (2011)
614 236–244.

615 [45] J. Reppenhagen, J. Werther, Catalyst attrition in cyclones, Powder
616 Technol. 113 (1–2) (2000) 55–69.

617 [46] G. R. McDowell, J. P. de Bono, On the micro mechanics of one-
618 dimensional normal compression, Géotechnique 63 (11) (2013) 895–908.

619 [47] K. J. Hanley, C. O'Sullivan, X. Huang, Particle-scale mechanics of sand
620 crushing in compression and shearing using DEM, Soils Found. 55 (5)
621 (2015) 1100–1112.

622 [48] A. V. Potapov, C. S. Campbell, Computer simulation of shear-induced
623 particle attrition, Powder Technol. 94 (2) (1997) 109–122.

[49] F. Fulchini, M. Ghadiri, A. Borissova, B. Amblard, S. Bertholin, A. Cloupet, M. Yazdanpanah, Development of a methodology for predicting particle attrition in a cyclone by CFD–DEM, Powder Technol. 357 (2019) 21–32.

[50] S. Plimpton, Fast parallel algorithms for short-range molecular dynamics, J. Comput. Phys. 117 (1) (1995) 1–19.

[51] E. J. Garboczi, Three-dimensional mathematical analysis of particle shape using X-ray tomography and spherical harmonics: Application to aggregates used in concrete, Cem. Concr. Res. 32 (10) (2002) 1621–1638.

[52] G. Arfken, Mathematical Methods for Physicists (second ed.), Academic Press, New York, 1970.

[53] C. Cohen-Tannoudji, B. Diu, F. Laloë, Quantum Mechanics: Volume I. Waves and particles. Introduction to the fundamental ideas of quantum mechanics, Wiley, 1977.

[54] B. Zhou, J. Wang, B. Zhao, Micromorphology characterization and reconstruction of sand particles using micro X-ray tomography and spherical harmonics, Eng. Geol. 184 (2015) 126–137.

[55] Z.-K. Feng, W.-J. Xu, R. Lubbe, Three-dimensional morphological characteristics of particles in nature and its application for DEM simulation, Powder Technol. 364 (2020) 635–646.

[56] M. Grigoriu, E. Garboczi, C. Kafali, Spherical harmonic-based random

fields for aggregates used in concrete, Powder Technol. 166 (3) (2006) 123–138.

[57] A. X. Jerves, R. Y. Kawamoto, J. E. Andrade, Effects of grain morphology on critical state: a computational analysis, Acta Geotech. 11 (2016) 493–503.

[58] Y. Feng, K. Han, D. Owen, Energy-conserving contact interaction models for arbitrarily shaped discrete elements, Comput. Methods Appl. Mech. Engrg. 205–208 (2012) 169–177.

[59] D. J. Evans, S. Murad, Singularity free algorithm for molecular dynamics simulation of rigid polyatomics, Mol. Phys. 34 (2) (1977) 327–331.

[60] G. Domokos, G. W. Gibbons, The evolution of pebble size and shape in space and time, P. Roy. Soc. Lond. A Mat. 468 (2146) (2012) 3059–3079.

[61] M. Ghadiri, Z. Zhang, Impact attrition of particulate solids. Part 1: A theoretical model of chipping, Chem. Eng. Sci. 57 (17) (2002) 3659–3669.

[62] F. Kun, H. J. Herrmann, Transition from damage to fragmentation in collision of solids, Phys. Rev. E 59 (3) (1999) 2623–2632.

[63] D. E. Grady, Length scales and size distributions in dynamic fragmentation, Int. J. Fract. 163 (2010) 85–99.

[64] D. J. Durian, H. Bideaud, P. Duringer, A. Schröder, F. Thalmann, C. M. Marques, What is in a pebble shape?, Phys. Rev. Lett. 97 (2) (2006) 028001.

667 [65] T. Szabó, G. Domokos, J. P. Grotzinger, D. J. Jerolmack, Reconstruct-
668 ing the transport history of pebbles on Mars, Nat. Commun. 6 (2015)
669 8366.

670 [66] P. H. Morris, D. J. Williams, A worldwide correlation for exponential
671 bed particle size variation in subaerial aqueous flows, Earth Surf. Proc.
672 Land. 24 (9) (1999) 835–847.

673 [67] J. J. Fedele, C. Paola, Similarity solutions for fluvial sediment fining by
674 selective deposition, J. Geophys. Res.-Earth 112 (2007) F02038.